

The Proper Motion of the Central Compact Object RX J0822–4300 in the Supernova Remnant Puppis A, Revisited

Martin Mayer¹, Werner Becker^{1,2}, Daniel Patnaude³, P. Frank Winkler⁴, and Ralph Kraft³, Max-Planck Institut für extraterrestrische Physik, Giessenbachstrasse, D-85741 Garching, Germany Max-Planck Institut für Radioastronomie, Auf dem Hügel 69, D-53121 Bonn, Germany Smithsonian Astrophysical Observatory, Cambridge, MA 02138, USA

4 Department of Physics, Middlebury College, Middlebury, VT 05753, USA

Received 2020 May 19; revised 2020 June 24; accepted 2020 June 28; published 2020 August 24

Abstract

We present an improved proper-motion measurement of the central compact object RX J0822–4300, located in the supernova remnant Puppis A. By employing a new data set taken in 2019 February by the High Resolution Camera on board the Chandra X-ray Observatory, we approximately double the available temporal baseline for our analysis to slightly more than 19 yr (7000 days). We correct for the astrometric inaccuracy of Chandra using calibrator stars with known optical positions that are detected in all observations. Thereby, we obtain absolute positions of RX J0822–4300 accurate to around 0.11 and from these a new best estimate for its total proper motion of $\mu_{\text{tot}} = (80.4 \pm 7.7)$ mas yr⁻¹. For a remnant distance of 2 kpc, this corresponds to a projected kick velocity of (763 ± 73) km s⁻¹ at a position angle of $\phi_0 = (247.8 \pm 4.4)^\circ$. The proper-motion measurement of RX J0822–4300 is used for discussing the kinematic age of Puppis A.

Unified Astronomy Thesaurus concepts: Neutron stars (1108); Compact objects (288); X-ray point sources (1270); Proper motions (1295); Pulsars (1306); Supernova remnants (1667); X-ray astronomy (1810)

1. Introduction

After their death in violent core-collapse supernovae (i.e., types Ib, Ic, II), massive stars leave behind compact remnants such as black holes or neutron stars. The latter constitute an opportunity to directly observe matter under some of the most extreme conditions in the universe. Over the years, observations have revealed a diverse "zoo" of neutron stars: while most young neutron stars are detected as nonthermal pulsed sources in the radio, optical, X-ray, or γ -ray regime (for an overview, see e.g., Becker 2009; Harding 2013), members of the class of Central Compact Objects (CCOs) are seen exclusively as isolated hot, steady thermal emitters in X-rays, located at (or near) the center of supernova remnants (SNRs), but without characteristic pulsar wind nebulae. In particular, CCOs have been found to be associated with relatively young, oxygen-rich Galactic remnants of core-collapse supernovae such as Cas A (Tananbaum 1999; Chakrabarty et al. 2001) and Puppis A (Petre et al. 1996). In total, the sample of Galactic SNRs with confirmed CCOs consists of around 10 objects, including G266.1-1.2, PKS 1209-51/52, G330.2+1.0, G347.3-0.5, G350.1-0.3, Kes 79, G353.6-0.7, and G15.9+0.2 (see De Luca 2017, and references therein).

While X-ray pulsations of CCOs have been detected in a few cases, these can be fully explained by the rotational modulation of thermal emission from hotspots on the neutron-star surface (e.g., Gotthelf et al. 2010) and are therefore not comparable to strong pulsations across the electromagnetic spectrum seen from typical young pulsars. The exact reason for the existence of these hotspots is still unclear, since heating through accretion or particle bombardment seems unlikely (De Luca 2017). The lack of nonthermal emission from CCOs can likely be attributed to their comparatively weak magnetic field, which is inferred from small spin-down rates, justifying their designation as

"anti-magnetars" (Gotthelf et al. 2013). An issue with the description of CCOs as a homogeneous class is the paucity of their descendants, since one would expect to find many more "orphaned" compact objects (Halpern & Gotthelf 2010) without visible SNRs in a similar region of the $P - \dot{P}$ parameter space than are observed in practice (Kaspi 2010).

The dynamical imprint of a violent supernova explosion on its remnant can be studied by observing the kinematics of the ejecta, e.g., fast-moving optical filaments, but also by studying the proper motion of the neutron star itself. Typically, contemporary simulations of core-collapse supernovae predict significant explosion asymmetries, which manifest themselves as bipolar jets, large-scale anisotropies, and/or strong natal kicks to the compact object. These birth kicks can be made plausible simply by conservation of momentum: if a large ejecta mass is expelled at high velocity, preferentially in a certain direction, one would naturally expect the compact remnant to experience recoil in the opposite direction.

After it was found from optical observations that ejecta in Puppis A generally expand toward north and east (Winkler & Kirshner 1985; Winkler et al. 1988), it was expected that a possible compact remnant would be moving toward the southwest. Following the discovery of the CCO RX J0822–4300 by Petre et al. (1996), the measurement of its kinematics thus became very interesting, even though it is challenging to achieve sufficient astrometric accuracy for an object that emits exclusively in X-rays. Such a study became possible only after the launch of Chandra owing to its unparalleled spatial resolution, once a sufficiently long temporal baseline of 5.3 yr (1999 December–2005 April) between observations had been acquired.

Two studies successfully measured a proper motion toward the southwest, with marginally consistent results for its absolute value: Hui & Becker (2006) found $\mu_{\rm tot} = (107 \pm 34)~{\rm mas~yr^{-1}},$ while Winkler & Petre (2007) measured an even larger value of $\mu_{\rm tot} = (165 \pm 25)~{\rm mas~yr^{-1}}.$ Combined with an approximate

See also http://www.iasf-milano.inaf.it/~deluca/cco/main.htm.

Table 1
Chandra Observations of RX J0822–4300

Instrument	strument ObsID Date		OnTime (s)	Exposure Time (s)	
HRC-I	749	1999 Dec 21/22	18014	9860	
HRC-I	4612	2005 Apr 25	40165	21317	
HRC-I	11819	2010 Aug 10/11	33681	15467	
HRC-I	12201	2010 Aug 11	38681	17808	
HRC-I	20741	2019 Feb 2	40175	19790	

Note. The 2010 observation was carried out as two consecutive ObsIDs (11819 and 12201), without intervening repointing (Becker et al. 2012). Therefore, we merged the two event files after the reprocessing step using dmmerge.

distance to the SNR of 2 kpc, the measurement by Winkler & Petre (2007) implied a very high transverse velocity on the order of 1600 $\rm\,km\,s^{-1}$, leading to the designation of RX J0822–4300 as a "cosmic cannonball." While constituting an exciting result on its own, this finding was in conflict not only with observations of pulsar birth velocities being on the order of $\sim\!500~\rm\,km\,s^{-1}$ (Caraveo 1993; Frail et al. 1994; Hobbs et al. 2005), but also with theoretical predictions from simulations of supernova explosions. However, Becker et al. (2012) repeated the above study including a new Chandra HRC observation taken in August 2010, and found a more conservative value of $\mu_{\rm tot}=(71\pm12)~\rm mas~yr^{-1}$, which corresponds to a velocity of (672 \pm 115) $\rm\,km~s^{-1}$, a result in better agreement with theory and the general distribution of measured pulsar proper-motion velocities.

In order to finally "pin down" the proper motion of RX J0822–4300 in direction and magnitude, this work incorporates a new Chandra observation from early 2019, almost doubling the previously available time baseline. In Section 2, we give an overview of the data set we used and the initial data processing. In Section 3, we describe the analysis steps we used to obtain the CCO proper-motion value from our data. We then discuss the implications for neutron-star kick velocity and remnant age in Section 4 and summarize our findings in Section 5.

2. Observations and Data Reduction

In total, RX J0822–4300 has been observed five times with Chandra's high-resolution camera (HRC). Four of these observations were taken with the HRC-I detector (optimized for imaging), and one with the HRC-S (optimized for spectroscopic readout). In order to reduce the influence of possible small but relevant systematic deviations between the detectors (e.g., due to differences in the degap correction or slight misalignments of the detector axes), we exclude the HRC-S observation from our analysis, leaving four observations spanning 19.18 yr. These consist of three archival observations, and a new one carried out on 2019 February 2. A journal of the relevant observation IDs, dates, and observation length is given in Table 1.

We acquired the archival observations from the Chandra Data Archive⁷ and reprocessed the data using the standard Chandra Interactive Analysis of Observations (CIAO Fruscione et al. 2006)

script chandra_repro to create new level 2 event files on which we base our proper-motion analysis. In this and all subsequent steps we used CIAO version 4.9 and *CALDB* version 4.7.4. We checked the observations for flares by inspecting the light curves of regions free of point sources. For the latest observation (ID 20741), we found a background flare affecting the data during around 8% of the time. Therefore, we excluded the affected time intervals for an effective exposure of 18,195 s, yielding a significantly reduced particle background while hardly affecting the number of source counts.

Based on the previous results, we can see that we need to achieve an absolute astrometric accuracy significantly below the level of one arcsecond in order to obtain sufficient precision on our measurement of the proper motion of the CCO. Therefore, while the absolute positional accuracy of Chandra is unparalleled for X-ray telescopes at $\sim 0.6^{10}$, we still have to improve on the raw astrometric position by a factor of a few in order to obtain a clean signal for the neutron-star motion. Our method closely follows that of Becker et al. (2012), albeit with some changes, which we will highlight in the next sections. As in the previous works on this topic, we use three nearby optical calibrator stars (designated as A, B, and C) that are detected in X-rays to obtain a precise reference for the world coordinate system (WCS). We take advantage of the Gaia DR2 catalog, which offers strongly improved precision on the positions and proper motions of our astrometric calibrators (Gaia Collaboration et al. 2016, 2018) compared to the UCAC3 catalog (Zacharias et al. 2010). In Table 2, we list the optical properties of the stars, and we indicate their relative location to RX J0822–4300 (designated as NS in the following) in Figure 1.

The X-ray image demonstrates the general difficulty of detecting weak point sources on top of diffuse background emission from the SNR. While being very faint in X-rays, source C is located in a region of relatively low diffuse emission and can therefore reliably be detected despite the low associated count rate. Source B, however, is superimposed on bright diffuse emission, which hampers its precise localization. Furthermore, all three calibrator sources are located well off-axis, where the Chandra point-spread function (PSF) becomes increasingly degraded. Comparing these limitations in the X-ray regime to the exquisite precision of the optical positions of the stars in the Gaia catalog, we can infer that the dominant error source will lie in the determination of source positions in X-rays, and not in the input astrometric calibration values.

As a first approximation, we use CIAO's wavelet detection algorithm wavdetect to estimate the positions and to verify the detectability of all calibrator sources in each observation. We then extract subimages centered on each source for each observation to reduce computation times in the subsequent steps. In order to not significantly oversample the PSF, we use bin sizes of 1×1 pixels for the NS, and 2×2 pixels for sources A, B, C. Since the calibrator sources are located well off-axis (where the PSF broadens) and have fewer counts compared to the CCO, we do not lose a significant amount of information with the 2×2 pixel binning and we suppress pixel-to-pixel fluctuations for the faint sources.

⁶ In the analysis of Becker et al. (2012), it was found that this high velocity was attributable to a subtle bug in the Chandra software for fitting and locating the off-axis reference stars. See Section 3.1 of this paper.

https://cda.harvard.edu/chaser/mainEntry.do.

⁸ http://cxc.harvard.edu/cal/ASPECT/celmon/

https://www.cosmos.esa.int/web/gaia/dr2

 Table 2

 IDs, Positions, and Proper Motions of the Three Reference Stars

Designation		Position (E	poch 2015.5)	Proper Motion	
Short	Gaia Source ID	R.A. (ICRS) (h:m:s)	Decl. (ICRS) (d:m:s)	μ_{lpha} (mas yr $^{-1}$)	μ_{δ} (mas yr ⁻¹)
A	5526323497671973632	08:21:46.2788	-43:02:03.590	-11.68 ± 0.03	2.70 ± 0.03
В	5526324631543374464	08:22:24.0044	-42:57:59.261	-0.35 ± 0.03	8.49 ± 0.03
C	5526323527726140416	08:21:48.8067	-43:01:28.211	-51.05 ± 0.04	6.82 ± 0.04

Note. Data as listed in the Gaia DR2 catalog (Gaia Collaboration et al. 2018). The stated 1σ uncertainties of R.A. and decl. at the reference epoch are significantly below the milliarcsecond level, and would only become relevant at the sixth and fifth decimal digits, respectively. The proper motions along the R.A. and decl. axes are labeled μ_{α} and μ_{δ} , respectively

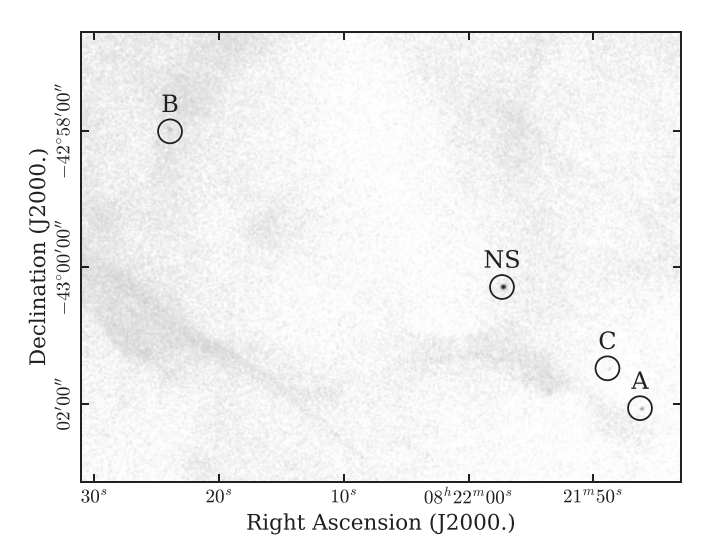


Figure 1. Image of the observation from 2010 with the positions of RX J0822–4300 and the astrometric calibrator stars indicated. The scale is logarithmic and the image has been slightly smoothed with a Gaussian of width $0\rlap.{''}5$. The field measures around $8\rlap.{'}8$ \times $6\rlap.{'}6$.

3. Spatial Analysis

In order to measure the proper motion of RX J0822–4300 from our data, we apply a method similar to that described in Becker et al. (2012): we determine the position of all sources (NS, A, B, C) in each data set by modeling and fitting an appropriate PSF to the data (Section 3.1). Combining the measured positions of the calibrator stars with their optical positions, we determine an optimal transformation from Chandra's coordinate system to the WCS, which we then apply to the X-ray position of the CCO. In this step, special care is taken in the propagation of uncertainties from each individual fit to the final corrected position of RX J0822-4300, effectively reducing the final size of the error contours (Section 3.2). From the absolute positions of the CCO at four epochs, we then straightforwardly determine a new best-fit estimate for its proper motion in two dimensions (Section 3.3).

3.1. PSF Modeling and Fitting

In order to get the most reliable estimate for the source positions, we simulate a PSF model for each source in each observation. This is necessary to get results that are unbiased by, e.g., the telescope roll angle and pointing, since the off-axis PSF is very broad, and more importantly, distorted. Therefore, the location of peak flux in the PSF does not necessarily correspond to the actual source

location. For our simulations, we used the online Chandra Ray Tracer tool (ChaRT), 10 which incorporates the best available model of the Chandra high-resolution mirror assembly (HRMA). ChaRT uses an input source position in combination with the aspect solution of the observation to trace the photon trajectories from the sky through the HRMA up to the detector plane. The key parameters are the assumed source monochromatic energy, which we set to 1.0 keV (see Becker et al. 2012) and the source photon flux, which we set to the maximal value of $1 \times 10^{-2} \, \text{cm}^{-2} \, \text{s}^{-1}$, in order to minimize the influence of Poisson fluctuations on our PSF model. PSF models with a lower simulated source flux may better resemble the actual images qualitatively, but quantitative fits performed with those yield underestimated positional errors and show larger systematic fluctuations. The ChaRT documentation explicitly discourages artificially scaling up source flux to create more rays. However, this warning applies mostly to simulations where one attempts to model nonlinear detection effects like photon pileup in CCD cameras. The HRC also experiences effects at high rates, such as count rate nonlinearity and deadtime effects, but these do not impact the imaging quality of the source. In total, we create five statistically independent simulations for each source.

The five ray files created by ChaRT are then fed simultaneously into MARX¹¹ (Davis et al. 2012, version 5.4.0), which we use to project the rays onto the HRC-I detector and to simulate its response to the photons. We finally obtain PSF model images for each source, with the respective binning matching the data. An impression of the morphology of the PSF models is given in the central panel of Figure 2. We found that, in order for the PSF to accurately reflect the observed image, we need to set the model detector behavior to "non-ideal." This applies additional blurring (induced by the HRC detector) to the PSF, leading to a closer match between model and data for on-axis sources than would be the case otherwise.

We would like to highlight two more subtle points. First, the PSF image is projected on a grid of sky pixels that exactly matches the pixel grid of the actual observation. Therefore, the "true" source position (i.e., the positional input into ChaRT) is not located exactly at the central pixel of the PSF image, but slightly offset from it by a subpixel margin. This offset is an effect that we later correct for by adding its value to the fitted position of the source. If we ignore this effect, we find deviations between fits of the same source at different image bin sizes.

http://cxc.harvard.edu/chart/index.html

¹¹ http://space.mit.edu/CXC/MARX/

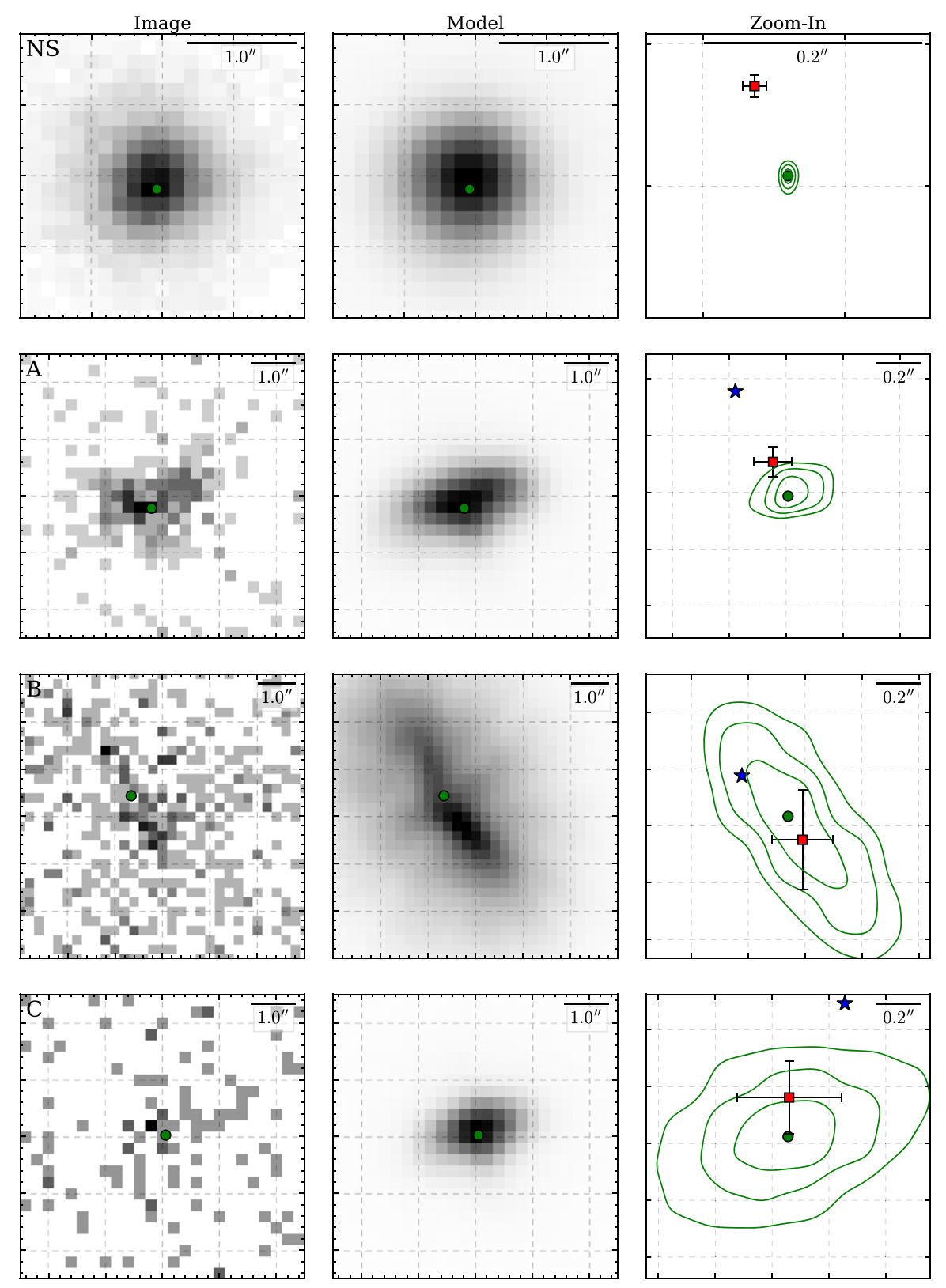


Figure 2. Illustration of the PSF fits for the four sources in the 2010 observation (ObsIDs 11819 and 12201). Left: input images; center: best-fit model, i.e., PSF image convolved with best-fit narrow Gaussian; right: zoom on the source position. We indicate the best-fit (x, y)-position (green circle; as in Table 3) with its 1σ , 2σ , and 3σ uncertainty contours returned by reg_proj. For comparison, we plot the raw best-fit position given in Becker et al. (2012) (red square) and the optical position from Gaia projected on our coordinate system (blue star). Data and model images have been binned by a factor of 2 for sources A, B, C and a square-root intensity scale was used to display them.

Second, when comparing the "true" source position for the PSF of the on-axis (off-axis angle <30") source with the location of the apparent centroid (or "center of mass") of the simulated PSF, we find that they do not coincide as perfectly as one would expect. Instead, there is a systematic offset on the order of 0."1, which always appears to point in the same direction on the detector even for different simulated roll angles. This behavior is also observed when performing the entire ray-tracing simulation with MARX only. The Chandra help desk confirmed that this behavior is unexpected, and probably indicative of the achievable limit on astrometric precision. The presence of subtle systematic effects at a subpixel level therefore must be considered with much care in our analysis.

In the next step, we fit the PSF models to the individual images of RX J0822–4300 and A, B, C using Sherpa, 12 a modeling and fitting package developed for Chandra (Freeman et al. 2001). We follow the thread "Accounting for PSF Effects in 2D Image Fitting," according to which we convolve the PSF Image (which is normalized to one) with a narrow Gaussian of fixed width, but free to vary in (x,y)-position and amplitude. Additionally, our model incorporates a small, spatially uniform background component across the relevant image area. The convolution with a Gaussian of finite width is necessary to perform meaningful interpolations between pixels so that non-integer position values are possible and the source position is not "quantized" to the grid of image pixels.

Due to the Poisson nature of the data, we use the fit statistic cstat, an implementation of Poisson likelihood that can in principle be used similarly to χ^2 for model comparison, but regardless of the number of counts per pixel. Furthermore, we use the differential evolution algorithm implemented as moncar for optimization. After performing the fit, we use the methods conf to get a rough estimate of fitting uncertainties, and reg_proj to obtain a precise view of the error contours (or equivalently the likelihood profile) in the (x,y)-plane.

During the refinement of the fit parameters, we noticed that the reference point for the convolution does not seem to naturally coincide with what we specify as the PSF center parameter. This behavior is very similar to the one produced by the CIAO software bug reported in Becker et al. (2012), which led to the extreme proper-motion velocity reported by Winkler & Petre (2007) and constitutes a potentially serious problem for the analysis of the fit results, since for off-axis sources this can result in an offset from the best-fit position by as much as a few pixels. Therefore, in order to actually "fixate" the center of the PSF, we additionally need to specify the hidden parameter origin, which makes the convolution process behave as expected. As an example, a complete impression of data and fitted models for a single observation (epoch 2010) is given in Figure 2. In Table 3, we list all best-fit positions for the individual epochs.

There are several things to note about the fitting process. First, as expected, the fitting of two of the calibrator sources proves to be difficult, due to the very high background emission (source B) and the quite limited photon statistics (source C). This makes the statistical errors on the astrometric calibration for these sources at least an order of magnitude larger than that for the fit of the CCO position on the detector.

Second, there are systematic offsets between the best-fit X-ray positions and the known optical positions for the stars. This proves that an astrometric correction is justified and needed in order to obtain the highest possible precision on the final result. Also, we would like to highlight that the uncertainties represented by the fit contours cannot be described well with simple independent Gaussian errors in *x* and *y*, since they show significant irregularities and interdependencies.

Finally, we observe small but significant deviations between our best-fit positions and the ones in Becker et al. (2012), most noticeably for the NS. This is probably related to differences between the actual PSF models fitted to the data, since it seems unlikely that the data are altered this drastically by our reprocessing. The differences between the two fits are found to be partly explainable by the deviations between the nominal centroid and center of mass of the PSF model, which we indicated earlier. At worst, this corresponds to a systematic error in the NS position of around 0."1, which could in principle severely bias our final proper-motion estimate. However, any minor coordinate offset that is constant over the detector or scales only linearly with x and y will naturally be compensated by our coordinate transformation in Section 3.2, since it would apply to all sources equally.

3.2. Transformation to the WCS

In principle, there are many ways imaginable to align the coordinate systems of the individual observations. However, given the small number of calibrators, we attempt only two very common types of transformations to the WCS, similar to those applied in Winkler & Petre (2007):

1. Translation: for each observation, we determine an optimal transformation with two degrees of freedom, corresponding to a simple coordinate offset $(\Delta x, \Delta y)$ in an arbitrary direction:

$$\begin{pmatrix} x' \\ y' \end{pmatrix} = \begin{pmatrix} x \\ y \end{pmatrix} + \begin{pmatrix} \Delta x \\ \Delta y \end{pmatrix}, \tag{1}$$

where x and y correspond to Chandra sky coordinates, and x' and y' represent WCS locations projected onto the sky coordinate system.

2. Scaling and rotation: in addition to the simple translation, we allow for a small scale factor of the coordinate system r and a rotation by a small angle θ :

$$\begin{pmatrix} x' \\ y' \end{pmatrix} = \begin{pmatrix} r\cos\theta & -r\sin\theta \\ r\sin\theta & r\cos\theta \end{pmatrix} \begin{pmatrix} x \\ y \end{pmatrix} + \begin{pmatrix} \Delta x \\ \Delta y \end{pmatrix}. \tag{2}$$

These two methods are analogous to the available modes of CIAO's standard wcs_match script. For the determination of the optimal transformation parameters, we weight all three calibrators evenly. Thereby, their "center of mass" is relatively close to the actual position of the NS (i.e., the location of the calibrators is not heavily biased toward a certain side of the detector).

Given that a simple Gaussian description of the error is likely an oversimplification, we choose a slightly different approach than Becker et al. (2012) to determine an absolute position of the NS: for each source, we take into account the values of the fit statistic on a finely spaced (x,y)-grid around the best fit,

http://cxc.harvard.edu/sherpa/

¹³ See https://cxc.cfa.harvard.edu/sherpa/statistics/.

 Table 3

 Optical and "raw" Fitted X-Ray Positions and Properties for All Sources at all Four Epochs

		Source	X-ray			Optical (Gaia DR2)	
ObsID	Epoch		R.A. (J2000.) (h:m:s)	Decl. (J2000.) (d:m:s)	Counts	R.A. (J2000.) (h:m:s)	Decl. (J2000.) (d:m:s)
749	1999.97	NS	08:21:57.4040(006)	-43:00:16.539(005)	3123		
		A	08:21:46.2906(049)	-43:02:03.308(132)	45	08:21:46.2953(0)	-43:02:03.632(0)
		В	08:22:24.0205(146)	-42:57:59.362(109)	109	08:22:24.0049(0)	-42:57:59.393(0)
		C	08:21:48.8703(103)	-43:01:28.104(180)	13	08:21:48.8790(1)	-43:01:28.316(1)
4612	2005.31	NS	08:21:57.3817(003)	-43:00:17.223(004)	6854		
		A	08:21:46.3002(052)	-43:02:03.919(042)	121	08:21:46.2896(0)	-43:02:03.618(0)
		В	08:22:24.0203(070)	-42:57:59.549(149)	178	08:22:24.0047(0)	-42:57:59.348(0)
		C	08:21:48.8849(130)	-43:01:28.597(178)	9	08:21:48.8542(0)	-43:01:28.280(0)
11819/12201	2010.61	NS	08:21:57.3262(002)	-43:00:17.463(005)	10490		
		A	08:21:46.2617(036)	-43:02:04.089(063)	199	08:21:46.2840(0)	-43:02:03.603(0)
		В	08:22:23.9851(111)	-42:57:59.491(225)	170	08:22:24.0046(0)	-42:57:59.303(0)
		C	08:21:48.8535(135)	-43:01:28.861(123)	19	08:21:48.8295(0)	-43:01:28.244(0)
20741	2019.09	NS	08:21:57.3078(003)	-43:00:17.017(004)	6208		
		A	08:21:46.3035(074)	-43:02:03.284(101)	81	08:21:46.2749(0)	-43:02:03.580(0)
		В	08:22:24.0607(339)	-42:57:58.841(193)	77	08:22:24.0043(0)	-42:57:59.231(0)
		C	08:21:48.8239(145)	-43:01:27.880(211)	18	08:21:48.7900(0)	-43:01:28.186(0)

Note. The X-ray positions shown here correspond to the best-fit source position in sky coordinates returned by Sherpa, uncorrected for any astrometric offsets. The errors on X-ray source positions correspond to the maximum one-sided 1σ error returned by the conf task and are therefore just a crude estimate of the associated uncertainties. For illustrative purposes, we also list rounded "errors" on the last digits of the optical positions, demonstrating that they are of very little importance for the overall uncertainty budget. The column "Counts" lists the amplitude of the Gaussian model which was convolved with the PSF. This therefore corresponds to an estimate for the number of source counts with subtracted background.

rather than propagating the best-fit and Gaussian uncertainties. The statistic values are extracted using the Sherpa task reg_proj. For each star i (i = A, B, C), the "C statistic" C_i corresponds to the twice the negative logarithm of the Poissonian likelihood \mathcal{L}_i . Therefore, we can obtain probability values $P_i(x, y)$ for the position of the star at every point on the grid around the best-fit value by normalizing the total likelihood to one:

$$P_{i}(x, y) = \frac{\mathcal{L}_{i}(x, y)}{\sum_{\hat{x}, \hat{y}} \mathcal{L}_{i}(\hat{x}, \hat{y})}$$

$$= \frac{\exp\left(-\frac{1}{2} C_{i}(x, y)\right)}{\sum_{\hat{x}, \hat{y}} \exp\left(-\frac{1}{2} C_{i}(\hat{x}, \hat{y})\right)},$$
(3)

where we implicitly assume a flat prior over our (x,y)-grid, i.e., all viable (and realistic) fit locations are assumed to be within the range of our grid.

From this, we can now propagate our fit uncertainties without making any strong assumptions on their shape. For the translation method, this is relatively straightforward if we space all our grid points evenly: for each star i, we take the differential between the Gaia location at (x', y') and the coordinates of the probability contours at (x,y) to obtain a distribution of translation vectors:

$$T_i(\Delta x, \Delta y) = P_i(x = x' - \Delta x, y = y' - \Delta y). \tag{4}$$

We then average over the three stars by convolving these distributions (corresponding to a summation of the components) and dividing the resulting translation vector by 3. We convolve this average distribution with the distribution for the NS location $P_{\rm NS}(x, y)$ to obtain an estimate of its corrected WCS location.

For the scaling and rotation method, we cannot use the same principle, since a rotation will automatically "mix" the x and y coordinates, so convolving them on a Cartesian grid is not sensible. Instead we use the following numerical Monte Carlo technique: for each of the four objects (NS, A, B, C), we sample $N = 10^6$ points (e.g., $x_{i,1}$, $x_{i,2}$,..., $x_{i,N}$) from their individual probability distributions $P_i(x, y)$. From the samples of A, B, C, we obtain a distribution of the four transformation parameters Δx_n , Δy_n , r_n , and θ_n by fitting them in Equation (2). This corresponds to solving the following equation in a standard least-squares manner for each of the N samples.

$$\begin{pmatrix} x_{A} & -y_{A} & 1 & 0 \\ y_{A} & x_{A} & 0 & 1 \\ x_{B} & -y_{B} & 1 & 0 \\ y_{B} & x_{B} & 0 & 1 \\ x_{C} & -y_{C} & 1 & 0 \\ y_{C} & x_{C} & 0 & 1 \end{pmatrix} \begin{pmatrix} r \cos \theta \\ r \sin \theta \\ \Delta x \\ \Delta y \end{pmatrix} \approx \begin{pmatrix} x'_{A} \\ y'_{A} \\ x'_{B} \\ y'_{B} \\ x'_{C} \\ y'_{C} \end{pmatrix}.$$
 (5)

We then apply the individual transformations as in Equation (2) to the simulated sample of neutron-star locations to obtain the probability distribution for its absolute location. This method automatically provides us with an estimate for the most likely location of the CCO and detailed uncertainty contours, since it takes into account all likely positions of the individual calibrators. In contrast, we found that standard Gaussian error propagation of only the diagonal elements of the covariance matrix for the transformation parameters leads to an overestimation of the final error on (x'_{NS}, y'_{NS}) , since the transformation parameter values are strongly dependent on each other (i.e., there are large off-diagonal elements in the covariance matrix).

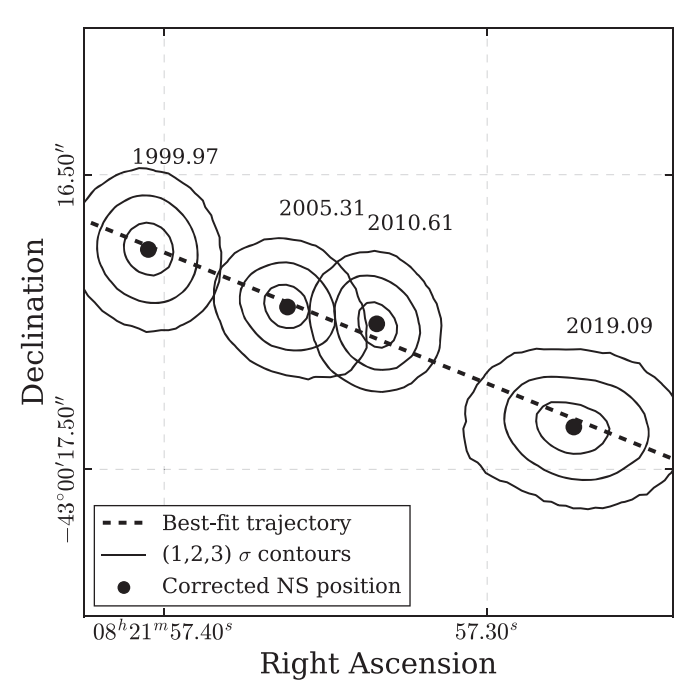


Figure 3. Motion of RX J0822–4300. We plot the absolute positions of the NS at the four epochs by indicating the mode and the 1σ , 2σ , and 3σ contours (i.e., the smallest regions containing the corresponding fractions of cumulative probability) derived from their distribution. In addition, we indicate the direction of motion (i.e., the best-fit position angle ϕ_0 as determined in Section 3.3) with a dashed line. This figure corresponds to an area of $2'' \times 2''$ on the sky.

By applying both methods to the PSF fits of each observation, and converting the resulting distributions from sky coordinates to celestial coordinates, 14 we get a clear impression of the motion of the CCO, as can be seen in Figure 3. Note that here, as in the following sections, we choose to plot the results from the scaling and rotation method, as it constitutes the more robust coordinate transformation, and its results barely differ from those from the translation method. The corresponding absolute positions, including uncertainties, are listed in Table 4 for both methods. Here, as everywhere else in this paper, listed uncertainty ranges correspond to the 68% central interval of the probability distribution of the respective quantity. Note that the relatively large uncertainty on the NS position in 2019 is caused by difficulties in the fitting of the position of source B. In that epoch, it is found to appear significantly fainter than in, e.g., the observation from 2005, despite having comparable exposure times.

3.3. The Proper Motion of RX J0822-4300

From the probability distributions for the NS position at four epochs spanning 19.18 yr, we can now determine the most likely value of its proper motion in a relatively straightforward way. We determine the best-fit values μ_{α} , μ_{δ} fulfilling the following equation, describing motion at constant speed in two dimensions:

$$\begin{pmatrix} \alpha(t) \\ \delta(t) \end{pmatrix} = \begin{pmatrix} \mu_{\alpha} \\ \mu_{\delta} \end{pmatrix} \cdot (t - t_0) + \begin{pmatrix} \alpha_0 \\ \delta_0 \end{pmatrix}, \tag{6}$$

Table 4Absolute Positions of RX J0822–4300

Epoch	Method	R.A. (J2000.) (h:m:s)	Decl. (J2000.) (d:m:s)
1999.97	Translation	$08:21:57.402^{+0.008}_{-0.008}$	$-43:00:16.70^{+0.07}_{-0.10}$
	Scaling and rotation	$08:21:57.405^{+0.008}_{-0.008}$	$-43:00:16.75^{+0.09}_{-0.09}$
2005.31	Translation	$08:21:57.360^{+0.008}_{-0.007}$	$-43:00:16.93^{+0.08}_{-0.07}$
	Scaling and rotation	$08:21:57.362^{+0.007}_{-0.007}$	$-43:00:16.95^{+0.07}_{-0.08}$
2010.61	Translation	$08:21:57.331^{+0.007}_{-0.008}$	$-43:00:17.00^{+0.07}_{-0.07}$
	Scaling and rotation	$08:21:57.334^{+0.007}_{-0.006}$	$-43:00:17.01^{+0.08}_{-0.08}$
2019.09	Translation	$08:21:57.271^{+0.014}_{-0.011}$	$-43:00:17.33^{+0.08}_{-0.09}$
	Scaling and rotation	$08:21:57.273^{+0.012}_{-0.011}$	$-43:00:17.36^{+0.09}_{-0.09}$

Note. We list the median values and 68% central intervals of the marginalized distributions for R.A. and decl. at the given epochs.

where we have introduced the labels α and δ for R.A. and decl., t describes the epoch of the observations in years (with $t_0=2019.09$, corresponding to the time of our latest observation), and α_0 , δ_0 correspond to the NS location at t_0 . We define μ_α such that a positive value describes an increase in R.A., i.e., motion from west to east.

In practice, we perform the fit by again drawing representative samples from the distributions for the individual epochs and then performing a least-squares fit for each sample, leading to a final distribution of proper-motion values in $(\mu_{\alpha}, \mu_{\delta})$ -space. With this method, we also obtain an absolute astrometric reference point (α_0, δ_0) for RX J0822–4300, corresponding to its position at the time of our latest observation (epoch 2019.09). By sampling simultaneously in α and δ , we include the effect of any possible interdependence between these parameters, even though the position contours in Figure 3 appear to be quite well behaved. We show representative one-dimensional projections onto the WCS axes of this fit (using the scaling and rotation method) in Figure 4 and display the corresponding distribution of proper-motion values in Figure 5.

The individual corrected positions at the four epochs agree well with the expected linear trajectory. Also, the probability distributions for the source locations and proper-motion components appear well behaved and can be described with reasonable accuracy by Gaussian distributions.

In order to exclude large systematic errors in our result due to a possibly biased PSF centroid (see Section 3.1), we also tried an alternative approach for the conversion of the fit results to the final proper-motion value, by taking the "center of mass" of the PSF image as the precise source location instead of its nominal centroid position. From this analysis, we obtained results that differ by only $\sim\!0.5$ mas yr $^{-1}$ from the ones shown here. This demonstrates that the effect of such minor potential offsets on the fit output can be balanced by our coordinate transformation method, which inherently compensates for linear distortions of the detector scale.

In order to extract more illustrative quantities from our measurement, we convert the proper motion vector to polar coordinates by defining the total proper motion, μ_{tot} , and the position angle east of north, ϕ_0 , as

$$\mu_{\text{tot}} = \sqrt{\mu_{\alpha}^2 + \mu_{\delta}^2} \tag{7}$$

$$\tan \phi_0 = \frac{\mu_\alpha}{\mu_\delta}.\tag{8}$$

¹⁴ Here, the term "sky coordinates" refers to a tangent-plane system aligned with celestial R.A. and decl., but measured in *pixels* (see https://cxc.cfa.harvard.edu/ciao/ahelp/coords.html).

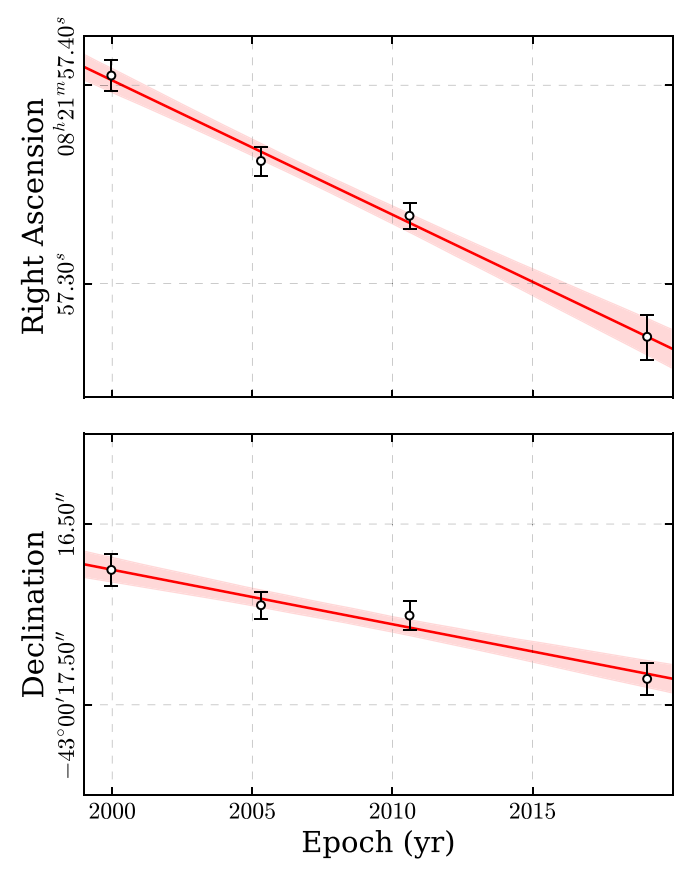


Figure 4. Fits to the proper motion of RX J0822–4300 projected onto the R.A. (top) and decl. (bottom) axes. We indicate the median (best-fit) trajectory with a thick red line, and the 68% central interval of possible trajectories as red shaded regions.

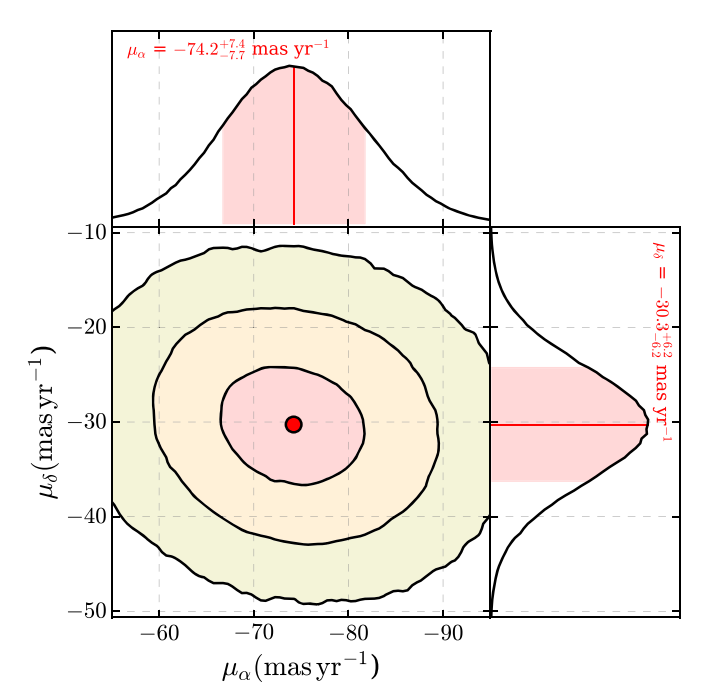


Figure 5. Two-dimensional distribution of the proper-motion vector $(\mu_{\alpha}, \mu_{\delta})$. We show the best fit (red circle) and the contours corresponding to the cumulative probability within 1σ , 2σ , and 3σ , respectively. In the top and right panels, we show the corresponding marginalized probability distributions for R.A. and decl. components of proper motion. We indicate the median values and 68% central intervals for the marginalized quantities in red.

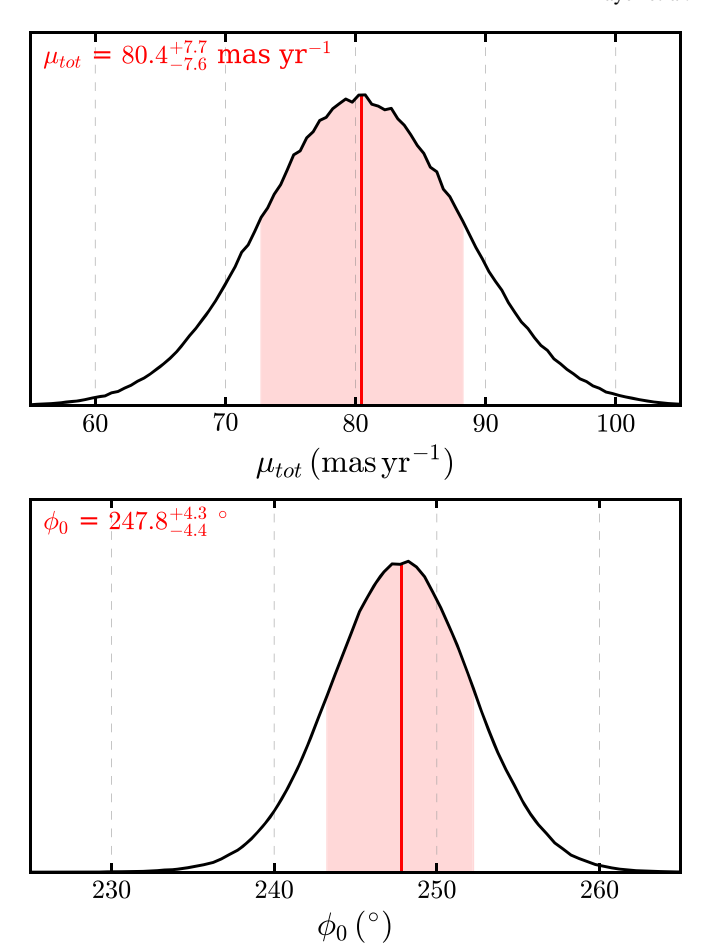


Figure 6. Top: marginalized distribution of the total proper motion $\mu_{\rm tot}$ with the median and 68% central interval indicated in red. Bottom: same for the position angle ϕ_0 .

By applying these simple relations to our sample of propermotion vectors, we obtain final probability distributions of the magnitude of the proper motion and of its direction, which we show in Figure 6.

We display the resulting astrometric solutions and uncertainties in Table 5. The results of the two transformation methods agree with each other. Since it constitutes the more robust coordinate transformation, we quote our proper motion from the scaling and rotation method as final: $\mu_{\rm tot}=80.4^{+7.7}_{-7.6}\,{\rm mas~yr^{-1}}$ and $\phi_0=247.8^{+4.3}_{-4.4}.$

In general, our values agree within uncertainties with those given in Becker et al. (2012) ($\mu_{\rm tot} = (71 \pm 12) \, {\rm mas \ yr^{-1}},$ $\phi_0 = (244 \pm 11)^{\rm o}$), with our median values corresponding to slightly higher proper motion and a slightly "shallower" position angle (when projected onto the sky). Naturally, our uncertainty on both values is smaller than theirs, since we have made use of a time baseline almost twice as long. Interestingly however, the relative increase in precision of the position angle is larger than that for the magnitude of proper motion. By looking at Figure 3, we can see that this is at least partly due to our position estimate for the observation from 2019, whose error contours are more extended along the direction of motion than perpendicular to it.

Gotthelf et al. (2013) use an alternative method to constrain the proper motion of RX J0822–4300: They determine the locations of the NS and calibrator stars by measuring their centroids of the observed images. They then correct the

Table 5Final Results for the Proper Motion of RX J0822–4300

Method	μ_{α} (mas.yr $^{-1}$)	μ_{δ} (mas.yr $^{-1}$)	μ_{tot} (mas.yr $^{-1}$)	φ ₀ (°)	$lpha_0$ (h:m:s)	δ_0 (d:m:s)
Translation Scaling and rotation	$-75.1_{-8.0}^{+7.7} \\ -74.2_{-7.7}^{+7.4}$	$-31.0^{+6.4}_{-6.3} \\ -30.3^{+6.2}_{-6.2}$	$81.6_{-7.5}^{+7.5} \\ 80.4_{-7.6}^{+7.7}$	$247.5_{-4.7}^{+4.7} 247.8_{-4.4}^{+4.3}$	$08:21:57.272^{+0.009}_{-0.010} \\08:21:57.274^{+0.009}_{-0.010}$	$-43:00:17.34_{-0.08}^{+0.08} \\ -43:00:17.33_{-0.08}^{+0.08}$

Note. The proper-motion values in this table correspond to the medians and 68% central intervals indicated in Figures 5 and 6. We provide (α_0, δ_0) as a reference point for the absolute astrometric position of RX J0822–4300 at the epoch of our latest observation (2019.09, MJD 58516.5).

resulting value by the offset between centroid and source positions, as measured from simulated PSF images. They use only star A as a calibrator source, since it is the brightest of the three stars. If we apply this method to our data set, we obtain a proper motion of (82 ± 7) mas yr⁻¹ at a position angle of $(249 \pm 4)^{\circ}$, entirely consistent with our result from PSF fitting.

While the statistical errors here are comparable with those from our method, the Gotthelf et al. (2013) centroid method uses only a single location on the detector to calibrate the astrometric reference frame, neglecting possible systematic distortions over the detector, which our scaling and rotation method includes. It is possible to extend this "corrected centroid" method to stars B and C, but this is nontrivial as it requires an iterative procedure, and it leads to increased statistical errors. We conclude that while both methods are consistent, our PSF fitting technique is the more robust one.

4. Discussion

4.1. Kinematics and Kick Mechanism

Our refined measurement of the proper motion of RX J0822–4300 agrees well with the results of Becker et al. (2012), while providing smaller error bars on its magnitude and position angle. Calculating the projected velocity of the neutron star tangential to the line of sight, $v_{\rm proj}$, at an assumed distance d, ¹⁵ we obtain

$$v_{\text{proj}} = 763_{-72}^{+73} \times \left(\frac{d}{2 \text{ kpc}}\right) \text{ km s}^{-1}.$$
 (9)

This in principle constitutes a lower limit on the kick that the neutron star experienced during the supernova explosion, and therefore an important constraint on supernova models. Generally, the conclusions on the kinematics of the system outlined by Becker et al. (2012) hold when considering our updated value. Depending on neutron-star mass $M_{\rm NS}$ and d, we obtain the following expressions for the tangential components (or lower limits) of momentum p and kinetic energy $E_{\rm kin}$ carried by the neutron star:

$$p = (2.12 \pm 0.20) \times 10^{41}$$
$$\times \left(\frac{d}{2 \text{ kpc}}\right) \left(\frac{M_{\text{NS}}}{1.4 M_{\odot}}\right) \text{g cm s}^{-1}$$
(10)

$$E_{\rm kin} = 8.1^{+1.6}_{-1.5} \times 10^{48} \times \left(\frac{d}{2 \text{ kpc}}\right)^2 \left(\frac{M_{\rm NS}}{1.4 M_{\odot}}\right) \text{ erg.}$$
 (11)

Assuming a neutron star of mass $1.4~M_{\odot}$ at a distance of 2 kpc, we obtain an estimate for the momentum of the CCO of $p=(2.12\pm0.20)\times10^{41}~{\rm g~cm~s^{-1}}$. This is consistent with the approximate momentum attributed to the ejecta, seen to be expanding toward the northeast as fast, optically emitting filaments (Winkler & Kirshner 1985; Winkler & Petre 2007). For the kinetic energy of the neutron star, we obtain $E_{\rm kin}=8.1^{+1.6}_{-1.5}\times10^{48}~{\rm erg}$, corresponding to a fraction $f\sim0.8\%$ of the energy released in a canonical core-collapse supernova explosion of $10^{51}~{\rm erg}$.

While older measurements suggest a distance of around 2.2 kpc to Puppis A (e.g., Reynoso et al. 2003), several recent investigations favor a considerably lower distance of around 1.3 kpc (Woermann et al. 2000; Aschenbach 2015; Reynoso et al. 2017). If we assume this lower distance, we obtain a significantly smaller projected velocity of ~ 500 km s⁻¹, in even better agreement with the upper end of the neutron-star velocity distribution (see, e.g., Hobbs et al. 2005). Furthermore, the inferred momentum and kinetic energy would be reduced accordingly to around $p\sim1.4\times10^{41}\,\mathrm{g~cm~s^{-1}}$ and $E_{\mathrm{kin}}\sim$ 3.4×10^{48} erg, respectively. Distance measurements to Galactic SNRs are inherently difficult, since most are based on measuring H I or OH absorption features in their (continuum) radio spectrum, and using the presence (or absence) of such features, together with Galactic rotation models, to place lower and upper limits on the distance. Alternative methods based on optical and/or X-ray absorption are typically at least as

In principle, natal kicks on neutron stars can occur, e.g., via asymmetric neutrino emission during the explosion or via asymmetric ejection of matter due to hydrodynamic instabilities. The latter scenario is supported by the observed relationship between total ejecta mass and neutron-star kick velocity (Bray & Eldridge 2016). Wongwathanarat et al. (2013) coined the term "gravitational tug-boat mechanism" for the underlying hydrodynamic mechanism: massive, slowly moving ejecta on the side opposite the most violent explosion exert a gravitational pull on the newly born neutron star. This results in possible kick velocities on the order of $\sim\!1000~{\rm km~s^{-1}}$ for strongly asymmetric explosions (Janka 2017). Therefore, our proper-motion estimate for RX J0822–4300, and the associated projected velocity are consistent with theoretical considerations for any reasonable assumption on the distance.

The hydrodynamic nature of the kick mechanism is supported by an investigation of the spin properties of RX J0822–4300: while the CCO exhibits pulsed emission at a period of 0.112 s, its origin is likely to be purely thermal, resulting from periodic modulation of blackbody emission from two antipodal hotspots on the neutron-star surface (Gotthelf & Halpern 2009; Gotthelf et al. 2010). The specific properties of these hotspots (temperature and effective area) lead to a

¹⁵ For the sake of comparability with earlier publications on this topic, we adopt a distance d=2 kpc as a reference scale.

phase-reversal of the pulse profile at an energy of around 1.2 keV, rendering the broadband detection of pulsed emission difficult. Through the analysis of phase-coherent timing observations, Gotthelf et al. (2013) were able to measure a total period derivative of $\dot{P}=(9.28\pm0.36)\times10^{-18}$ for the pulses of RX J0822–4300. After consideration of the kinematic contribution of the neutron-star motion via the Shklovskii effect (Shklovskii 1970), they derived a magnetic field of around 2.9 \times 10 derived and a "spin-down age" corresponding to \sim 2.5 \times 10 derived yr.

The latter quantity is, of course, an unrealistic age estimate, which shows that the implicit assumption of the neutron star being born rotating much faster than today is wrong for this object. In conjunction with the very weak magnetic field they inferred, this contradicts electromagnetic powering of the kick mechanism. That would require the newly born neutron star to rotate very fast or exhibit a very large magnetic field (Lai 2001). The low magnetic field and small period derivative are shared with other members of the CCO class, thus justifying their designation as "anti-magnetars" (Gotthelf et al. 2013). A possible explanation for the weak observed dipole field could be that it has been buried by rapid fallback accretion of supernova ejecta after the explosion, and only slowly diffuses back to the surface on a timescale of around 10^4 yr (Bogdanov 2014; Luo et al. 2015).

4.2. Age of Puppis A

By extrapolating the motion of the neutron star back in time, our revised proper-motion measurement of RX J0822-4300 also provides an updated estimate for the age of Puppis A. Winkler et al. (1988) analyzed the motion of faint, oxygen-rich filaments of the SNR in the optical. They found expansion at very high velocities (up to 1500 km s⁻¹) from a common center located at $\alpha(J2000) = 08^{\text{h}}22^{\text{m}}27^{\text{s}}.5, \delta(J2000) = -42^{\circ}57'29''$. The semimajor axis of the 68% confidence ellipse on this position is oriented almost exactly along the line toward the CCO (position angle $\phi = 242^{\circ}$ east of north), and measures 56"; the semiminor axis is 34" in the transverse direction. 16 Under the assumption of undecelerated trajectories for these dense knots, this center can be considered an estimate for the supernova explosion site. Assuming the errors on the expansion center to be approximately Gaussian, and comparing the coordinates of the expansion center with the position of the CCO in 2019, $(\alpha \approx 08^{\rm h}21^{\rm m}57^{\rm s}3, \delta \approx -43^{\circ}00'17'', \text{ Table 5})$, we find that the neutron star is located at an angular distance of $372'' \pm 37''$ from the expansion center determined by Winkler et al. (1988). The inferred direction of motion is $243^{\circ} \pm 4^{\circ}$, which overlaps, within the errors, with the position angle we measured for the proper motion of RX J0822-4300 in X-rays. We illustrate its past trajectory and the location of the optical expansion center in Figure 7.

By weighting our sample of trajectories (Figure 5), according to their likelihood of overlap with the observed expansion center and determining the amount of time needed for the CCO to cover the observed angular distance given the respective proper motion, we obtain an estimate for the kinematic age τ of Puppis A:

$$\tau = 4.6^{+0.7}_{-0.6} \times 10^3 \,\text{yr}.$$
 (12)

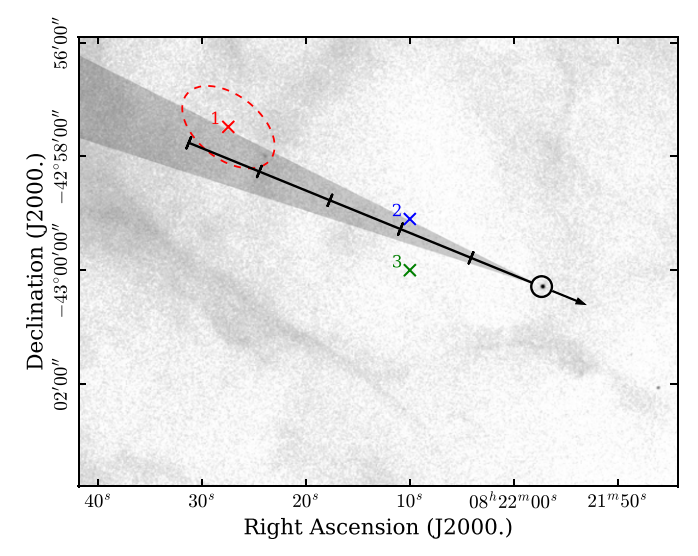


Figure 7. X-ray image of the central region of Puppis A with the past trajectory of RX J0822–4300 and directional uncertainties indicated. The optical expansion center of Winkler et al. (1988) and its 68% confidence ellipse are indicated in red and marked as 1. We also show the location of the alternative remnant center provided by Aschenbach (2015) and the remnant center obtained from radio data (see Green 2019), which are marked as 2 and 3, respectively. For RX J0822–4300, we mark the distance traveled every 1000 yr with increments.

This value is somewhat greater than the SNR age inferred from motion of the optical filaments alone, which Winkler et al. (1988) found to be $(3.7 \pm 0.3) \times 10^3 \,\mathrm{yr}$, though the two values agree within the errors. The errors in the total displacement and position angle of the NS from its origin, and in the age of the SNR, are dominated by uncertainties in the expansion center for the system of ejecta filaments.

The neutron star itself is unlikely to have experienced any past deceleration, while the optically visible ejecta might have, due to their far lower density. Therefore, including a uniform deceleration model for the ejecta could possibly increase the minor tension between the two measurements, since the age inferred from optical filaments alone would then be reduced. As Winkler et al. (1988) already noted, the apparent center of the radio shell is offset from the optical expansion center by $\sim 4'$ toward the southwest. Therefore, it may be worthwhile to consider that the actual explosion site might be located closer to RX J0822–4300 than inferred, which would lead to a lower measured age from neutron-star proper motion.

Aschenbach (2015) proposes to include an ejecta deceleration model that is not radially symmetric, but allows for different degrees of deceleration along two perpendicular axes. Repeating his approach with our updated proper-motion value, the inferred age would be radically reduced by a factor \sim 2.4 to around 1950 yr. ¹⁷ The implied location of the remnant center would then be at $\alpha = 08^{\rm h}22^{\rm m}10^{\rm s}.0$, $\delta = -42^{\circ}59'06''$, lying within one arcminute of the center of the radio shell of the SNR as given in the Green catalog (Green 2019). While the exact methodology may be a matter of debate here, this example highlights how strongly the kinematic age estimate can be systematically affected by input assumptions, such as an assumed (or neglected) deceleration model.

¹⁶ The 68% error ellipse comes from an updated analysis of the original data, and is (naturally) smaller than the 90% confidence ellipse shown in Winkler et al. (1988).

 $^{^{17}}$ Aschenbach (2015) originally stated an age of (1990 \pm 150) yr, based on the proper motion of Becker et al. (2012), which enters into his calculations explicitly.

4.3. Proper Motion Measurements of Other CCOs

Proper motion studies of neutron stars are generally a powerful tool for inferring their origin and age as well as the kinematics of the supernova explosion. For radio pulsars, such measurements exist in large numbers, allowing for statistical studies of their distribution (e.g., Hobbs et al. 2005). However, for neutron stars without radio emission, particularly CCOs, there are few such measurements, due to the paucity of objects and the challenging nature of such measurements at other wavelengths.

Apart from the measurement here and in previous works for RX J0822–4300, X-ray proper-motion results have been reported for three other CCOs, all with much lower transverse velocities than that of RX J0822–4300. For 1E 1207.4–5209, located in the SNR PKS 1209–51/52, Halpern & Gotthelf (2015) measured a relatively small proper motion of (15 \pm 7) mas yr $^{-1}$, $\nu_{\rm proj}$ < 180 km s $^{-1}$ for a distance of 2 kpc. For CXO J232327.8+584842 in Cas A, DeLaney & Satterfield (2013) measured a marginally significant projected velocity of (390 \pm 400) km s $^{-1}$ for a distance of 3.4 kpc, which corresponds to a proper motion of (24 \pm 25) mas yr $^{-1}$. Lastly, for the proper motion of CXO J085201.4-461753 in the Vela Jr. SNR (G266.2–1.2), only a 3σ upper limit of <300 mas yr $^{-1}$, corresponding to <1400 km s $^{-1}$ for a distance upper limit of 1 kpc, could be determined (Mignani et al. 2019). The latter two cases suffered from a lack of nearby calibrator sources, explaining their relatively large statistical errors.

All this illustrates that in order to perform proper-motion measurements of CCOs to similar precision as in this work, the temporal baseline covered by the data must be quite long, the object should be located relatively nearby, and there must be astrometric calibrator sources in the field of view.

5. Summary

We have incorporated a new Chandra observation of the central region of Puppis A to perform the most precise proper motion measurement of RX J0822–4300 to date. In particular, we have generalized the treatment of positional errors and used all available information from optical calibrator stars to obtain reliable position estimates and errors at all epochs. Our results are consistent within errors with those of Becker et al. (2012). We obtain a projected velocity of 763^{+73}_{-72} km s⁻¹, for a distance of 2 kpc to Puppis A. While this value lies on the upper end of the observed neutron-star velocity distribution, it does not pose a challenge for theoretical supernova models, since such speeds are achievable with hydrodynamical kick mechanisms. If the actual distance to Puppis A is smaller, as recent measurements suggest, then the velocity will become proportionally smaller as well.

The direction of neutron-star motion is consistent with the measurement of the supernova explosion site from optical filament expansion by Winkler et al. (1988). Our new measurement of the proper motion implies an age of 4600^{+700}_{-600} yr for the remnant, which is somewhat older than that derived from proper motions of the optical filaments alone. An important pillar for our age determination of Puppis A is the location of the optical center of expansion. The best currently available estimate is now over 30 yr old and was based on digitization of photographic plates from three epochs over a total baseline of only 8 yr. An updated measurement of the proper motions for the ejecta filaments based on CCD images, ideally from several epochs over an extended baseline, is long overdue. Images for such a measurement are in

hand, and the results will be reported separately (P. F. Winkler et al. 2020, in preparation). If one then finds a significant disagreement between the age based on the motion of optical filaments and that from extrapolation of the neutron-star trajectory, this could point toward nonballistic motion of the supernova ejecta clumps due to their interaction with the surrounding ISM.

We acknowledge multiple contributions by Rob Petre to the early stages of the work reported here. His history with RX J0822-4300 dates to the Einstein Observatory era, when he suspected the existence of a point source within Puppis A, even before its formal discovery in ROSAT data (Petre et al. 1982, 1996). M.M. acknowledges support by the International Max-Planck Research School on Astrophysics at the Ludwig-Maximilians University, IMPRS. P.F.W. acknowledges support from the NSF through grant AST-1714281 and from NASA through grant GO6-17064C. We acknowledge the use of the Chandra data archive and we are thankful for support by the Chandra help desk at various stages of our analysis. This work has made use of data from the European Space Agency (ESA) mission Gaia (https://www.cosmos.esa.int/gaia), processed by the Gaia Data Processing and Analysis Consortium (DPAC, https://www.cosmos.esa.int/web/gaia/dpac/consortium). Funding for the DPAC has been provided by national institutions, in particular the institutions participating in the Gaia Multilateral Agreement.

ORCID iDs

Martin Mayer https://orcid.org/0000-0002-9771-9841
Werner Becker https://orcid.org/0000-0003-1173-6964
Daniel Patnaude https://orcid.org/0000-0002-7507-8115
P. Frank Winkler https://orcid.org/0000-0001-6311-277X
Ralph Kraft https://orcid.org/0000-0002-0765-0511

```
References
Aschenbach, B. 2015, in Proc. of the XI Multifrequency Behaviour of
   High Energy Cosmic Sources Workshop (MULTIF15), 21, doi: 10.22323/
   1.246.0021
Becker, W. 2009, Neutron Stars and Pulsars, Astrophysics and Space Science
  Library, 357 (Berlin: Springer), 91
Becker, W., Prinz, T., Winkler, P. F., et al. 2012, ApJ, 755, 141
Bogdanov, S. 2014, ApJ, 790, 94
Bray, J. C., & Eldridge, J. J. 2016, MNRAS, 461, 3747
Caraveo, P. A. 1993, ApJL, 415, L111
Chakrabarty, D., Pivovaroff, M. J., Hernquist, L. E., Heyl, J. S., & Narayan, R.
   2001, ApJ, 548, 800
Davis, J. E., Bautz, M. W., Dewey, D., et al. 2012, Proc. SPIE, 8443, 84431A
De Luca, A. 2017, JPhCS, 932, 012006
DeLaney, T., & Satterfield, J. 2013, arXiv:1307.3539
Frail, D. A., Goss, W. M., & Whiteoak, J. B. Z. 1994, ApJ, 437, 781
Freeman, P., Doe, S., & Siemiginowska, A. 2001, Proc. SPIE, 4477, 76
Fruscione, A., et al. 2006, Proc. SPIE, 6270, 62701V
Gaia Collaboration, Brown, A. G. A., Vallenari, A., et al. 2018, A&A, 616, A1
Gaia Collaboration, Prusti, T., de Bruijne, J. H. J., et al. 2016, A&A, 595, A1
Gotthelf, E. V., & Halpern, J. P. 2009, ApJL, 695, L35
Gotthelf, E. V., Halpern, J. P., & Alford, J. 2013, ApJ, 765, 58
Gotthelf, E. V., Perna, R., & Halpern, J. P. 2010, ApJ, 724, 1316
Green, D. A. 2019, JApA, 40, 36
Halpern, J. P., & Gotthelf, E. V. 2010, ApJ, 709, 436
Halpern, J. P., & Gotthelf, E. V. 2015, ApJ, 812, 61
Harding, A. K. 2013, FrPhy, 8, 679
Hobbs, G., Lorimer, D. R., Lyne, A. G., & Kramer, M. 2005, MNRAS,
   360, 974
Hui, C. Y., & Becker, W. 2006, A&A, 457, L33
Janka, H.-T. 2017, ApJ, 837, 84
Kaspi, V. M. 2010, PNAS, 107, 7147
Lai, D. 2001, Physics of Neutron Star Interiors, 578, 424
```

Luo, J., Ng, C.-Y., Ho, W. C. G., et al. 2015, ApJ, 808, 130 Mignani, R. P., De Luca, A., Zharikov, S., et al. 2019, MNRAS, 486, 5716 Petre, R., Becker, C. M., & Winkler, P. F. 1996, ApJL, 465, L43 Petre, R., Kriss, G. A., Winkler, P. F., et al. 1982, ApJ, 258, 22 Reynoso, E. M., Cichowolski, S., & Walsh, A. J. 2017, MNRAS, 464, 3029 Reynoso, E. M., Green, A. J., Johnston, S., et al. 2003, MNRAS, 345, 671 Shklovskii, I. S. 1970, SvA, 13, 562 Tananbaum, H. 1999, IAUC, 7246, 1

Winkler, P. F., & Kirshner, R. P. 1985, ApJ, 299, 981
Winkler, P. F., & Petre, R. 2007, ApJ, 670, 635
Winkler, P. F., Tuttle, J. H., Kirshner, R. P., & Irwin, M. J. 1988, in IAU
Coll. 101, Supernova Remnants and the Interstellar Medium, ed.
R. S. Roger & T. L. Landecker (Cambridge: Cambridge Univ. Press), 65
Woermann, B., Gaylard, M. J., & Otrupcek, R. 2000, MNRAS, 317, 421
Wongwathanarat, A., Janka, H.-T., & Müller, E. 2013, A&A, 552, A126
Zacharias, N., Finch, C., Girard, T., et al. 2010, AJ, 139, 2184